Journal of Volcanology and Geothermal Research 387 (2019) 106671

Contents lists available at ScienceDirect

Journal of Volcanology and Geothermal Research

journal homepage: www.elsevier.com/locate/jvolgeores

Interferometric synthetic aperture radar study of recent eruptive activity at Shrub mud volcano, Alaska

Yufen Niu [a,b], Daniel Dzurisin [c], Zhong Lu [b,*]

[a] School of Geology Engineering and Geomatics, Chang'an University, Xi'an 710054, China
[b] Huffington Department of Earth Sciences, Southern Methodist University, Dallas, TX 75275, USA
[c] David A. Johnston Cascades Volcano Observatory, U.S. Geological Survey, Vancouver, WA 98683-9589, USA

ARTICLE INFO

Article history:
Received 22 May 2019
Received in revised form 5 September 2019
Accepted 5 September 2019
Available online 06 September 2019

Keywords:
InSAR
Modeling
Volume change
Mud volcano
Shrub
Alaska

ABSTRACT

Shrub mud volcano is one of three large mud volcanoes that comprise the Klawasi Group in the Copper River Basin of southcentral Alaska. Except for minor discharges in the mid-1950s when the group was first described, Shrub was dormant prior to its reactivation in summer 1996. From 1997 to 1999, Shrub vigorously erupted more than 5×10^5 m^3 of saline mud and CO_2-rich gas at temperatures as high as 54 °C. Thereafter, activity waned but continued at least through 2015. We analyzed 192 interferograms derived from 106 synthetic aperture radar (SAR) images acquired by the JERS-1 (L-band), ERS-1/2 (C-band), RADARSAT-1 (C-band), and ALOS PALSAR (L-band) satellites to characterize ground deformation at Shrub before, during, and after its reactivation. Collectively, the interferograms span 1992–2000 and 2006–2011. We fit the observations with two deformation sources: a deflating, steeply-dipping, pipe-like body under the summit area and an inflating, shallow-dipping, sill-like body under the southwest flank. Both sources are shallow, with centroids less than 1 km beneath the summit. Prior to reactivation, the flank source inflated ~0.35×10^5 m^3/yr from July 1992 to May 1996. During eruptive activity, the summit source deflated at higher rates that peaked at ~8.71×10^5 m^3/yr during May–November 1997 and continued at ~0.95×10^5 m^3/yr during the 2006–2011 observation window. Cumulative source-volume loss is comparable to the volume of mud erupted. We interpret the summit source as the volcano's feeder conduit that pressurized prior to the first SAR observation in 1992. Also before 1992, the conduit ruptured to feed a lateral intrusion of mud under the southwest flank, perhaps along a bedding plane in underlying glaciolacustrine deposits. The growing sill caused the southwest flank to inflate while it accommodated the mud supply from depth, which explains why we observed pre-eruptive inflation of the flank but not the summit. The summit began deflating when the conduit ruptured to the surface at the onset of eruptive activity. The flank source did not deflate concurrently because the weight of the thin overburden was insufficient to collapse the sill. There is a suggestion in the modern topography that lateral intrusions under Shrub's southwest flank are a common feature of activity there.

1. Introduction

Hundreds of mud volcanoes of various shapes and sizes have been identified on land and several thousand are assumed to exist on the seafloor (Kioka and Ashi, 2015; Mazzini and Etiope, 2017). Many occur in association with hydrocarbon-bearing basins, fold-and-thrust belts, or accretionary wedges at subduction zones, where they are interpreted as surface expressions of piercement structures rooted in deep-seated over-pressured sediments (Bishop, 1978; Brown, 1990; Kopf, 2002; Vanderkluysen et al., 2014). Methane (CH_4) is the most abundant gas species emitted, with lesser amounts of carbon dioxide (CO_2) and nitrogen (Brown, 1990; Hedberg, 1974; Kopf, 2002).

Mazzini and Etiope (2017) applied the term "sedimentary volcanism" to the process that produces such features, and drew a distinction between these and similar features that occur in association with active magmatic or hydrothermal systems, such as those at Mount Etna, Italy (Chiodini et al., 1996), in California and Nevada, USA (White, 1955), and in Yellowstone National Park, USA (Sheppard et al., 1992). They defined mud volcanoes as "…surface expressions of focused fluid flow inside hydrocarbon-bearing sedimentary basins" and challenged use of the term to describe similar features in magmatic or hydrothermal settings, for which they did not propose alternative terminology. Adding to the nomenclature quandary is the fact that many features at Yellowstone's well-known but inaptly-named Mud Volcano area are not mud volcanoes by any definition, but rather mud cauldrons, fumaroles, warm springs, and cool springs (Pitt and Hutchinson, 1982). Here we adopt the widely-used moniker "Shrub mud volcano" and

* Corresponding author.
E-mail address: zhonglu@smu.edu (Z. Lu).

https://doi.org/10.1016/j.jvolgeores.2019.106671
0377-0273/

the generic term "mud volcano" for descriptive purposes, without genetic connotation.

Like their magmatic counterparts, some mud volcanoes erupt continuously while others are quiescent for long periods between eruptions. Quiescence can be interrupted by a paroxysmal event such as a large earthquake, which can trigger copious release of mud and gases from deeply buried sediments (Mazzini et al., 2009; Mazzini et al., 2007; Mellors et al., 2007; Wang and Manga, 2010). In other cases, including the reactivation of Shrub in 1996, the immediate cause of renewed eruptive activity is ambiguous.

Mud volcanoes Upper Klawasi, Lower Klawasi, and Shrub comprise the Klawasi Group in the Copper River Basin of Wrangell-St. Elias National Park and Preserve in southcentral Alaska (Fig. 1). The features rise 50–100 m above surrounding terrain (~800 m base level) and are constructed of material from underlying glaciolacustrine deposits (Richter et al., 1998). Based on helium and carbon isotopic ratios, copious CO_2 emitted by the group is likely derived both by exsolution from a magmatic intrusive body and through contact metamorphism of limestone beds underlying the area (Motyka et al., 1989).

The Klawasi Group was first described by Nichols and Yehle (1961), who observed several small pools with minor mud and gas emissions on the southwest flank of Shrub during a visit in 1955; activity had declined somewhat by the following year. No activity nor any indication of recent activity was observed during a visit to Shrub in 1991, which led Richter et al. (1998, p. 4) to infer the feature had been "virtually inactive for many years." The earliest report of renewed activity came from a helicopter pilot who noted an active mud spring low on the north flank of the cone and activity at the summit during an overflight in summer 1996 (Richter et al., 1998). The following spring, Shrub began to vigorously erupt CO_2-rich gas and saline mud. The most active area in June 1997 was near the summit, where large amounts of gas and mud at 43 °C were discharging from a 65-m-long east-trending fissure. By August 1997, the fissure was nearly inactive but vigorous mud and gas emission at temperatures as high as 46 °C continued from vents at the summit and on the north, northwest, and southeast flanks of the cone. Dead vegetation to heights of two meters above the ground surface indicated that CO_2 had flowed down the flanks as streams in several locations. Small mammals and birds had perished around several of the CO_2 vents (Richter et al., 1998). In July 1998, mud and gas discharge was less violent, but the rate of mud production was about the same as in August 1997 (McGimsey et al., 2004). The same was true in June 1999, except activity was somewhat more widespread than in the previous two years and temperatures as high as 54 °C were measured (McGimsey et al., 2004; Sorey et al., 2000). Thereafter, sporadic observations suggest the intensity of activity declined, although the Alaska Volcano Observatory reported that activity "similar to that in 1999" continued at least through 2015 (https://www.avo.alaska.edu/volcanoes/activity.php?volcname=Klawasi%20Group&eruptionid=340&page=basic).

Many magmatic eruptions are preceded by a period of surface inflation (i.e., uplift and tumescence) caused by pressurization of a magma reservoir beneath the volcano (e.g., Dvorak and Dzurisin (1997); Lu et al. (2007)). Therefore, surface deformation measurements are important for understanding volcanic processes and hazards, and they can provide important insights into the structure, plumbing, and state of restless magmatic volcanoes. However, deformation associated with mud volcanism has not been well studied.

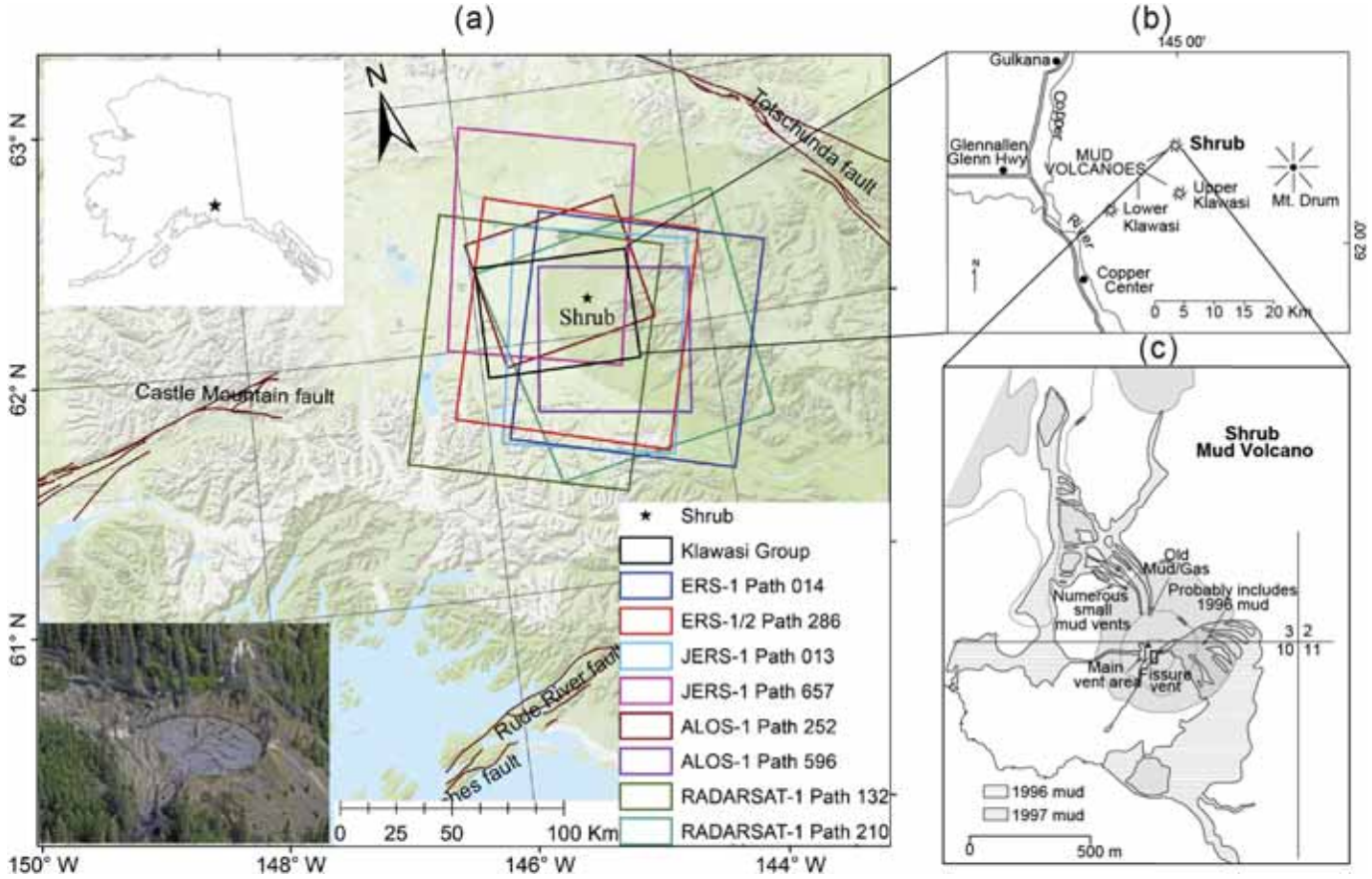

Fig. 1. (a) Map showing location of the Klawasi Group mud volcanoes in south-central Alaska (inset, upper left). Base map is from the ArcGIS online World Topography Map. Aerial photograph of Shrub mud volcano in 2009 (lower left) is from the Alaska Volcano Observatory. Colored rectangles indicate SAR satellites and paths for images used in this study. (b) Location map for Shrub, Lower Klawasi, and Upper Klawasi mud volcanoes that comprise the Klawasi Group (Richter et al., 1998). (c) Sketch map showing major CO_2 and mud vents at Shrub mud volcano, and distribution of mud deposits (McGimsey et al., 2004; Richter et al., 1998).

There is no dedicated ground-based monitoring network at Shrub or any of the Klawasi mud volcanoes. This makes the application of satellite-based monitoring techniques highly desirable. (Patrick et al., 2004) used a Landsat 7 Enhanced Thematic Mapper Plus (ETM+) image acquired on September 30, 2000, to estimate temperature, area of active mud discharge, and heat flux at Upper Klawasi and Lower Klawasi. Any thermal anomaly at Shrub was below the sensor's detection threshold. We are aware of no other remote sensing studies of the Klawasi Group prior to this study.

2. InSAR data and analysis

2.1. Data and processing approach

Interferometric synthetic aperture radar (InSAR) combines two or more SAR images of the same area acquired at different times from nearly the same vantage point to map any surface deformation that occurred during the time interval spanned by the images (Massonnet and Feigl, 1998; Mazzini and Etiope, 2017). InSAR has proven to be a useful tool for observing volcano deformation and interpreting magma-supply dynamic(e.g., Amelung et al. (2000); Biggs et al. (2010); Lu et al. (2010); Pagli et al. (2012); Pritchard and Simons (2004); Wicks et al. (2002); Wright et al. (2006)), and for estimating lava-flow thickness and extrusion rate (e.g., Lu et al. (2005); Ebmeier et al. (2012)). However, the technique has been applied only sparingly at mud volcanoes, including several in Azerbaijan (Antonielli et al., 2014; Hommels et al., 2003; Mellors et al., 2005) and LUSI in East Java, Indonesia (Abidin et al., 2009; Aoki and Sidiq, 2014; Fukushima et al., 2009; Rudolph et al., 2013). Given InSAR's success for studying diverse deformation mechanisms at numerous magmatic volcanoes in Alaska's Aleutian arc (Lu and Dzurisin, 2014), we applied the technique to Shrub mud volcano to determine if its reactivation in 1996 was preceded or accompanied by measurable surface deformation.

We obtained 106 ERS-1, ERS-2, JERS-1, RADARSAT-1 and ALOS PALSAR1 SAR images suitable for measuring surface deformation at Shrub (Table. 1, Fig. 1a).There is a gap in coverage between the last ERS-1/2 observation in May 2000 and the first ALOS PALSAR observation in May 2006. We used the two-pass InSAR approach (Massonnet and Feigl, 1998; Rosen et al., 2000) to produce 192 interferograms with reasonably good coherence using GAMMA software (www.gamma-rs.ch). The digital elevation model (DEM) used to produce the interferograms was derived from the "ALOS World 3D" (AW3D) system, with a pixel spacing of 1 arc-second (approximately 15 m × 30 m at Shrub) and vertical error of less than 6 m (Santillan and Makinano-Santillan, 2016). For each image pair, we optimized the Doppler centroid during SAR image generation. The average Doppler centroid of the two images was used to process the SAR signal data into single-look complex images from which the interferograms were produced (e.g., Lu and Dzurisin, 2014). Because the accuracy of the satellite state vectors provided in JERS-1 metadata is not as good as that for ERS-1 and ERS-2, we refined baselines of JERS-1 interferograms based on the fringe frequency in flat areas (Lu and Dzurisin (2014)). In part because the SAR data are from 8 different satellite paths and the degree of InSAR coherence varies among interferograms, our attempts to analyze the results using the persistent scatters technique or small baseline subset (SBAS) technique (e.g., Hooper (2008)) are unsuccessful. Instead, we analyzed and modeled individual interferograms and used the results to construct a time-series of source-volume changes as a function of time.

2.2. Results and analysis

The InSAR images show inflation of Shrub's southwest flank from the first SAR observation in 1992 until mid-1996. For example, more than 1 interferometric fringe corresponding to range shortening appears in 1993–1995 interferograms from C-band ERS-1 path 014 (Fig. 2a, b), about 1/4 fringe in a 1995–1996 interferogram from C-band ERS-2 path 286 (c), and about 1/3 fringe in 1992–1995 interferograms (d, e) and a 1992–1996 interferogram (f) from L-band JERS-1. One fringe corresponds to 2.83 cm of line-of-sight (LOS) surface displacement in the C-band interferograms, and 11.75 cm in the L-band interferograms. We conclude that the surface inflated about 1 cm from 1992 to 1993, almost 3 cm from 1993 to 1995, and nearly 0.7 cm from 1995 to 1996. The LOS displacement field was centered about 800 m southwest of Shrub's summit.

At the same time, a small amount of subsidence occurred on the east flank of the volcano (faint red tones east of summit in Fig. 2). Because the phase-change pattern shows up consistently in interferograms that span different time periods from both ERS-1/2 and JERS-1, we attribute it to surface subsidence rather than atmospheric path-delay effects. However, because the amount of subsidence is barely detectable and not well characterized by the interferograms, we did not attempt to account for it in source models.

Interferograms for the period 1996–1999 show Shrub's summit area deflated rapidly starting in mid-1996. For example, about 3 fringes surround the cone in a September 1996–September 1997 ERS-1/2 interferogram (Fig. 3a), about 2 fringes in a September 1996–August 1997 RADARSAT-1 interferogram (Fig. 3c), about 2.5 fringes in two 1996–1998 JERS-1 interferograms (June 1996–August 1998 and July 1996–June 1998) (Fig. 3e, g), and about 1 fringe in two 1997 88-day JERS-1 interferograms (03 July 1997–29 September 1997 and 04 July 1997–30 September 1997) (Fig. 3f, h). Collectively, the interferograms show the summit area deflated about 35 cm from summer 1996 to summer 1998 at time-varying rates that peaked at ~5 cm/month during July–September 1997. Deflation slowed somewhat in 1998 but continued at least until September 1999 (Fig. 3b). The center of the displacement field is offset about 200 m westward in the single ascending-path interferogram (Fig. 3d) compared to the descending-path interferograms. We attribute the shift to an inward, horizontal component of motion during eruptive activity. The effect is especially clear in the JERS-1/2 images owing to their relatively shallow incidence angle (Table 1) that provides more sensitivity to horizontal motion.

Summit subsidence continued during the 2006–2011 observation window, as shown by ALOS PALSAR interferograms from both ascending and descending paths (Fig. 4). For ascending paths, about half fringe surrounds the cone in an October 2006–July 2008 interferogram (Fig. 4a), about 1/4 fringe in a July 2007–July 2008 interferogram (Fig. 4b), about one fringe in a July 2007–June 2010 interferogram (Fig. 4c), about half fringe in a July 2008–September 2009 interferogram

Table 1
List of SAR images.

Sensors	Path	Frame	Incidence angle (°)	Heading angle (°)	Start date dd/mm/yy	End date dd/mm/yy	No. of images	No. of interferograms
ERS1	014	295	23.2	−165.1	11/07/1992	02/10/1995	9	15
ERS1/2	286	295	23.2	−165.1	03/06/1995	28/05/2000	15	29
JERS-1	013	295	38.8	−168.9	07/09/1992	16/09/1998	18	32
JERS-1	657	295	38.9	−168.5	08/09/1992	21/06/1998	19	34
RadarSAT-1	132	295	28.0	−165.3	02/09/1996	05/10/1999	2	1
RadarSAT-1	210	155	28.8	−14.2	10/08/1997	03/09/1997	2	1
ALOS-1	252	1240	38.8	−10.8	29/05/2006	12/03/2011	29	65
ALOS-1	596	2370	47.4	−171.7	04/06/2006	31/07/2010	12	15

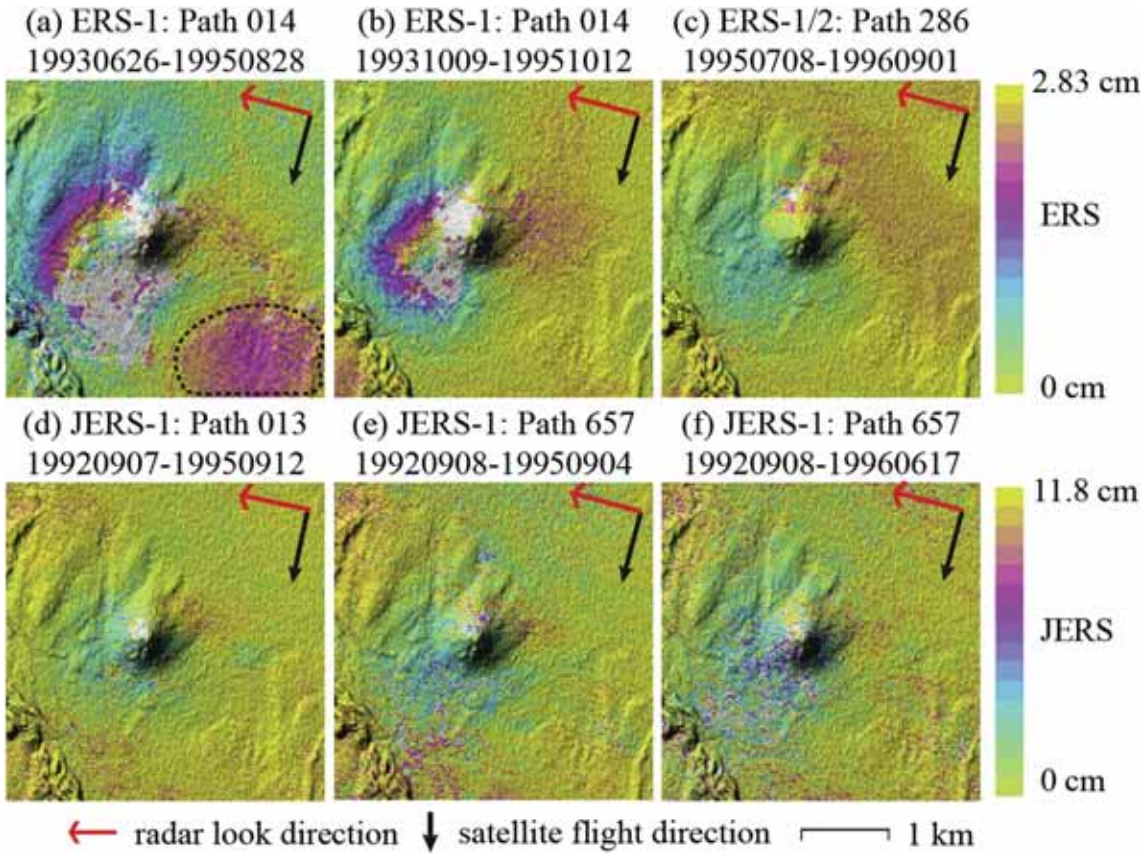

Fig. 2. Examples of interferograms showing deformation of Shrub volcano during 1992–1996, prior to its reactivation in June 1996. Data source and dates of SAR acquisitions are shown above each interferogram, e.g., for (a), ERS-1: Path 014 19930626-19950828 indicates ERS-1 path 014 with SAR acquisition dates of 26 June 1993 and 28 August 1995. (a) and (b) are from ERS-1 path 014 and span ~2 years each; (c), ERS-2 path 286, ~1.2 years; (d), JERS-1 path 013, ~3 years; (e) and (f) JERS-1 path 657, ~3 years and ~2.8 years, respectively. The strong phase-change signal in the southeast corner of (a) does not appear in other interferograms that span similar time periods and is almost surely an atmospheric artifact.

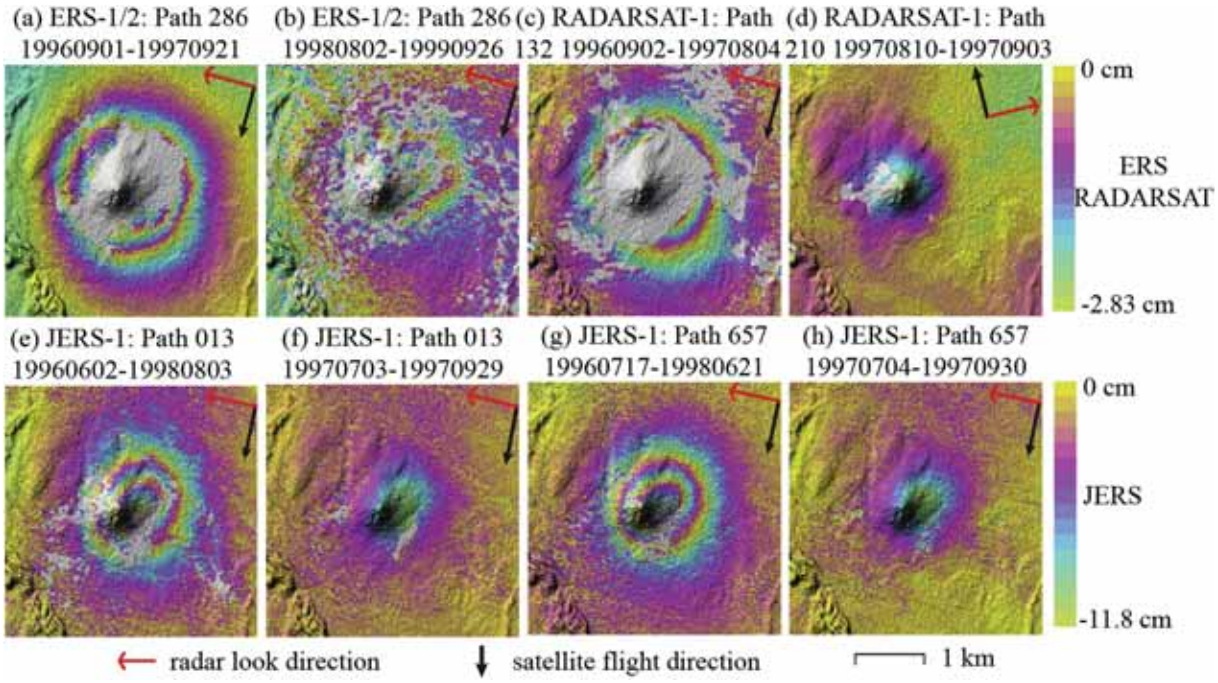

Fig. 3. Examples of interferograms showing deformation of Shrub volcano between 1996 and 2000 during the activity period: (a) and (b) are ERS1 path 286 pairs between 1996/09–1997/09 (~1 year) and 1998/08–1999/09 (~1.1 years); (c) is RADARSAT-1 path 132 pair between 1996/09–1997/08 (~0.9 year); (d) is RADARSAT-1 path 210 pair between 1997/08–1997/09 (~1 month); (e) and (f) are JERS path 013 pairs between 1996/06–1998/08 (~2.1 year) and 1997/07–1997/09 (~3 months); (g) and (h) are JERS path 657 pairs between 1996/07–1998/06 (~1.9 year) and 1997/07–1997/09 (~2 months). Note, (d) is the only ascending interferogram during 1992–2000.

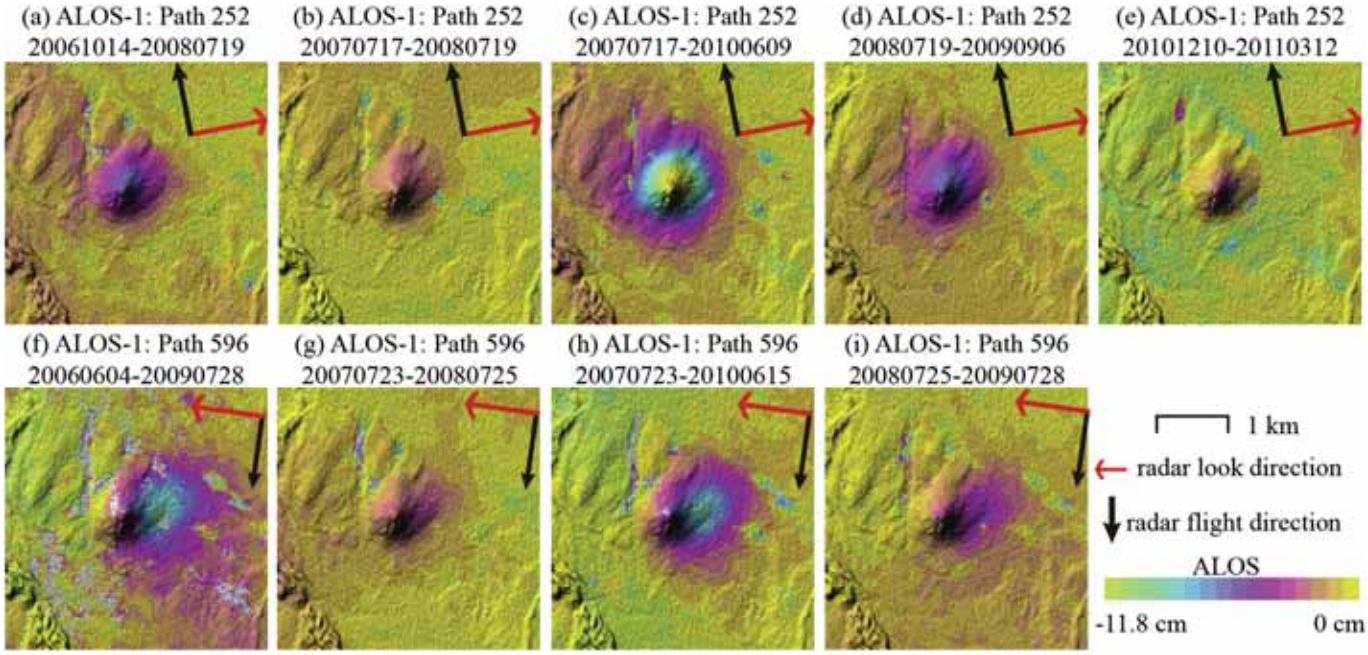

Fig. 4. Examples of interferograms showing deformation of Shrub volcano between 2006 and 2011 during the post-activity period: (a)–(e) are ascending ALOS PALSAR path 252 pairs between 2006/10–2008/07(~0.8 years), 2007/07–2008/07 (~1 years), 2007/07–2010/06 (~2.9 years), 2008/07–2009/09 (~1.2 years) and 2010/12–2011/03 (~3 month), respectively; (f)–(i) are descending ALOS PALSAR path 596 pairs between 2006/06–2009/07 (~3.1 years), 2007/07–2008/07 (~1 years), 2007/07–2010/06 (~2.9 years) and 2008/07–2009/07 (~1 years), respectively.

(Fig. 4d), and about 1/5 fringe in a December 2010–March 2011 interferogram (Fig. 4e). For descending paths, about 3/4 fringe surrounds the cone in October 2006–July 2009 interferogram (Fig. 4f), about 1/4 fringe in a July 2007–July 2008 interferogram (Fig. 4g), about one fringe in a July 2007–June 2010 interferogram (Fig. 4h), and about 1/3 fringe in a July 2008–July 2009 interferogram (Fig. 4i). As is the case for RADARSAT-1 interferograms, possibly due to the projection from three-dimensional surface displacement to LOS displacement, the surface displacement center is offset about 200 m to the west in ALOS PALSAR ascending interferograms (Fig. 4a–e) relative to descending interferograms (Fig. 4f–i).

We observed that interferometric coherence is better and persists longer at L-band than at C-band, consistent with results from InSAR investigations elsewhere (e.g., Lu et al. (2005)). For example, coherence is better in 1992–1995 and 1992–1996 L-band interferograms (Fig. 2d–f) than in 1993–1995 C-band interferograms (Fig. 2a, b). At C-band (ERS-1 and RADARSAT-1), interferometric coherence near the summit is maintained for short periods (e.g., 24 days, Fig. 3d), but lost in interferograms that span most of an entire year or more (Fig. 3a–c). The situation is better at L-band (JERS-1/2) (Fig. 3e–h); in some cases, good coherence persists for two years or more (e.g., Fig. 3e, g).

Inspection of all 192 interferograms, which span time periods ranging from several months to 6 years, leads us to the following conclusions concerning the persistence of interferometric coherence:

1. Coherence over Shrub and its surroundings is maintained as much as 2 years at C-band and 6 years at L-band if the SAR images are acquired during summer or early fall.
2. During periods of eruptive activity at Shrub, InSAR coherence is higher on the flanks than near the summit, especially at C-band. This is likely due to rapid surface changes caused by mud and gas discharge focused in the summit area during 1996–2000 and 2006–2011.
3. The degree of interferometric coherence depends strongly on image acquisition time. Best coherence is produced from images collected during the period of May to October, when snow and ice cover is minimal at Shrub.

3. Modeling and interpretation

3.1. Source models and approach

The simple shape and radially symmetrical pattern of both pre-eruptive and coeruptive deformation patterns (Figs. 2–4) suggest the plumbing system beneath Shrub comprises two primary sources, one beneath the volcano's southwest flank and another under the summit area. For its simplicity and flexibility, we chose the Yang prolate ellipsoid model (Yang et al., 1988) to represent summit source, i.e., a dipping, pressurized, prolate ellipsoidal cavity in an elastic half-space, and chose the penny-shaped crack model (Fialko et al., 2001) to represent the source under the southwest flank. With least-squares adjustment of a few parameters, the Yang model can approximate a range of volcanic sources, such as a relatively equant magma reservoir or a closed pipe-like conduit, while the penny-shaped crack can approximate a sill-like body (see Battaglia et al. (2013) for analytical expressions and software implementation).

The Yang model has been used with good success to model deformation at diverse magmatic volcanoes ranging from basaltic shields (e.g., Yang et al. (1992)) to rhyolitic caldera systems (e.g., Tiampo et al. (2000); Fialko and Simons (2001); Battaglia et al. (2003); Langbein (2003)). We considered other source models including variations of a vertical pipe (Bonaccorso and Davis, 1999) for the summit source and a circular tensional dislocation (penny-shaped crack) (Fialko et al., 2001) for the flank source. In our judgement the constraints provided by InSAR observations alone, lacking additional constraints from GPS or other geodetic data, do not justify a thorough investigation of alternative source models. Our goal is to gain first-order insights into the plumbing system at Shrub, and the prolate ellipsoid model and penny-shaped crack model are adequate for that purpose.

The prolate ellipsoid source is characterized by eight parameters, three spatial coordinates of the spheroid center x, y and z (north, south, and depth), major and minor axes of the spheroid a and b (the third axis of the spheroid is equal to the minor axis b), strike and dip of the major axis ϕ and θ, and the pressure change within the spheroid

ΔP (Battaglia et al., 2013; Yang et al., 1988). And the horizontal penny-shaped crack model is defined by five parameters: the spatial location of the crack center x, y and z (north, south, and depth), the crack radius r and the pressure change ΔP.

For each interferogram, we used Monte Carlo simulations (Binder et al., 1993) and the downhill simplex method to estimate optimal model parameters and uncertainties (Lu et al., 2005; Lu et al., 2003). The root mean-square error (RMSE) between observed and modeled interferograms is used as the prediction fit criterion. The volume change of summit source (Yang prolate ellipsoid model) is calculated with Eq. (1), derived by (Tiampo et al., 2000), using the optimal model parameters:

$$\Delta V = \Delta P a b^2 \pi / \mu \quad (1)$$

where ΔV is volume change, ΔP is pressure change, and μ is the shear modulus (Lame´ constant). And the volume change of southwest flank source (penny-shaped crack) is estimated using Fialko's Penny-shaped crack Matlab code (Fialko et al., 2001).

At Shrub, we assumed the shear modulus as 10 GPa and Poisson's ratio as 0.25 in a homogeneous isotropic elastic half-space both for the penny crack model and the prolate ellipsoid model. To account for topographic effects, we used a simple method proposed by Williams and Wadge (1998) in which source depth is adjusted at each computation point based on the point's elevation with respect to a reference surface. We chose the summit of Shrub volcano (900 m above sea level; ~100 m above surrounding terrain) as the reference elevation for modeled source depths.

3.2. Modeling of individual interferograms

As a first step, we modeled all 192 interferograms to assess the extent to which the modeled sources cluster in space or vary in time. We modeled 44 interferograms for the pre-eruptive period and 148 for the coeruptive period; results are shown in Fig. 5a. Modeled source locations cluster on the volcano's southwest flank during the pre-eruptive inflation period (red symbols) and near the summit during the coeruptive deflation period (black symbols). The clusters do not overlap, suggesting pre-eruptive flank inflation and coeruptive summit deflation were sourced differently. Within each cluster the pattern of source locations appears to be random in time, i.e., we saw no evidence for lateral migration of either source during the period of study. Neither did we see any systematic change in the best-fitting model parameters that would indicate significant changes in the source geometries over time.

To refine a best-fit model for each source, we selected subsets of high-quality pre-eruptive and coeruptive interferograms. Rates of ground deformation prior to reactivation in 1996 were small (0.7–1.5 cm/yr) relative to C-band and L-band wavelengths (~5.6 cm and 23.5 cm, respectively), so any deformation signal in pre-eruptive interferograms could be contaminated by atmospheric artifacts of comparable or greater magnitude. To mitigate the problem, we selected 20 of the 44 pre-eruption interferograms that each span at least 6 months,

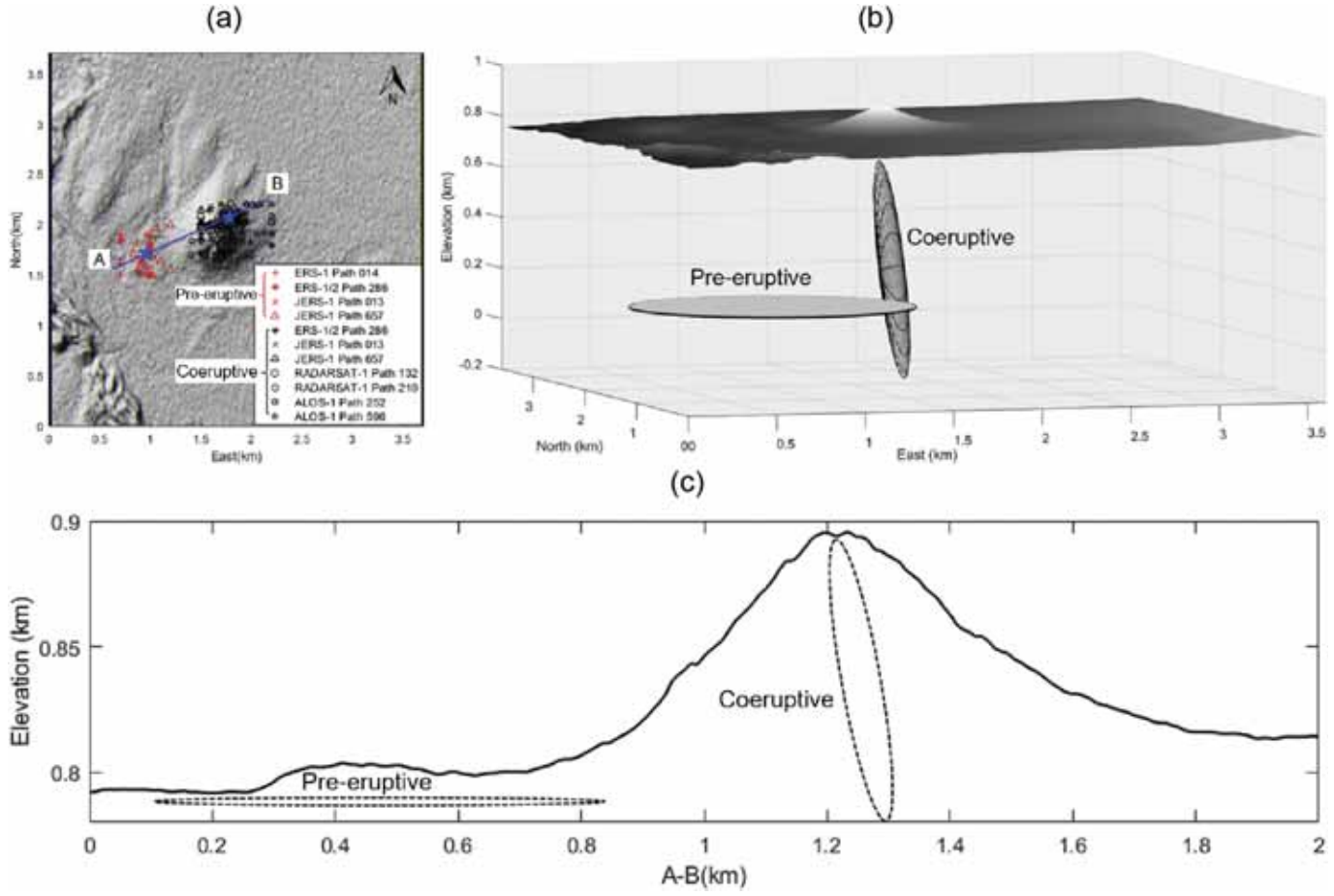

Fig. 5. (a) Horizontal locations of deformation sources for each of 192 interferograms analyzed in this study (44 pre-eruptive, 148 coeruptive), using the prolate ellipsoid model for coeruption penny-shaped crack model for pre-eruption. (b) Three-dimensional geometry of best-fit prolate ellipsoid sources for pre-eruptive and coeruptive time periods, obtained from 20 high-quality pre-eruptive interferograms and 115 high-quality coeruptive interferograms. See text for selection criteria and details of the modeling strategy. (c) WSW-ENE topographic profile along line A–B in (a). Locations of best-fit sources are shown schematically to illustrate relation to topographic features, i.e., depths and sizes are not accurate.

Table 2
Parameters for the best-fitting model based on the average of source models from selected interferograms: 20 for the pre-eruptive period and 115 for the coeruptive period.

Parameters	East (km)	North (km)	Depth (km)	Major axis (km)	Minor axis (km)	Strike(°)	Dip (°)
Before	0.85 ± 0.08	1.76 ± 0.09	0.74 ± 0.08	0.25 ± 0.23	0.007 ± 0.007	70 ± 6	18 ± 14
During	1.74 ± 0.22	2.02 ± 0.12	0.65 ± 0.26	0.44 ± 0.24	0.07 ± 0.08	97 ± 17	86 ± 7

Note: the horizontal origin of coordinates is the left bottom (shown in Fig. 5a), and the depth is estimated below the summit of Shrub mud volcano.

have good coherence, and exhibit a consistent phase anomaly pattern. Coeruptive deformation signals are larger, so any atmospheric contamination in those interferograms is less problematic and a greater proportion of the interferograms met our selection criteria. Of 148 coeruptive interferograms, 115 met our criteria and were used to refine the coeruptive source model.

For each subset of high-quality interferograms and the associated source models, we calculated average model parameters and their uncertainties (standard deviation) (Table 2). The standard deviation of each parameter in Table 2 was calculated by the 135 models based on the 135 selected interferograms. Then we remodel all 192 interferograms (44 pre-eruptive, 148 coeruptive) using the average horizontal source location for each subset. The resulting best-fit models are a sill-like source beneath the southwest flank (Fig. 5b) for the pre-eruptive period, and a nearly vertical, pipe-like source beneath the summit area (Fig. 5b) for the coeruptive period. Both sources are shallow, with

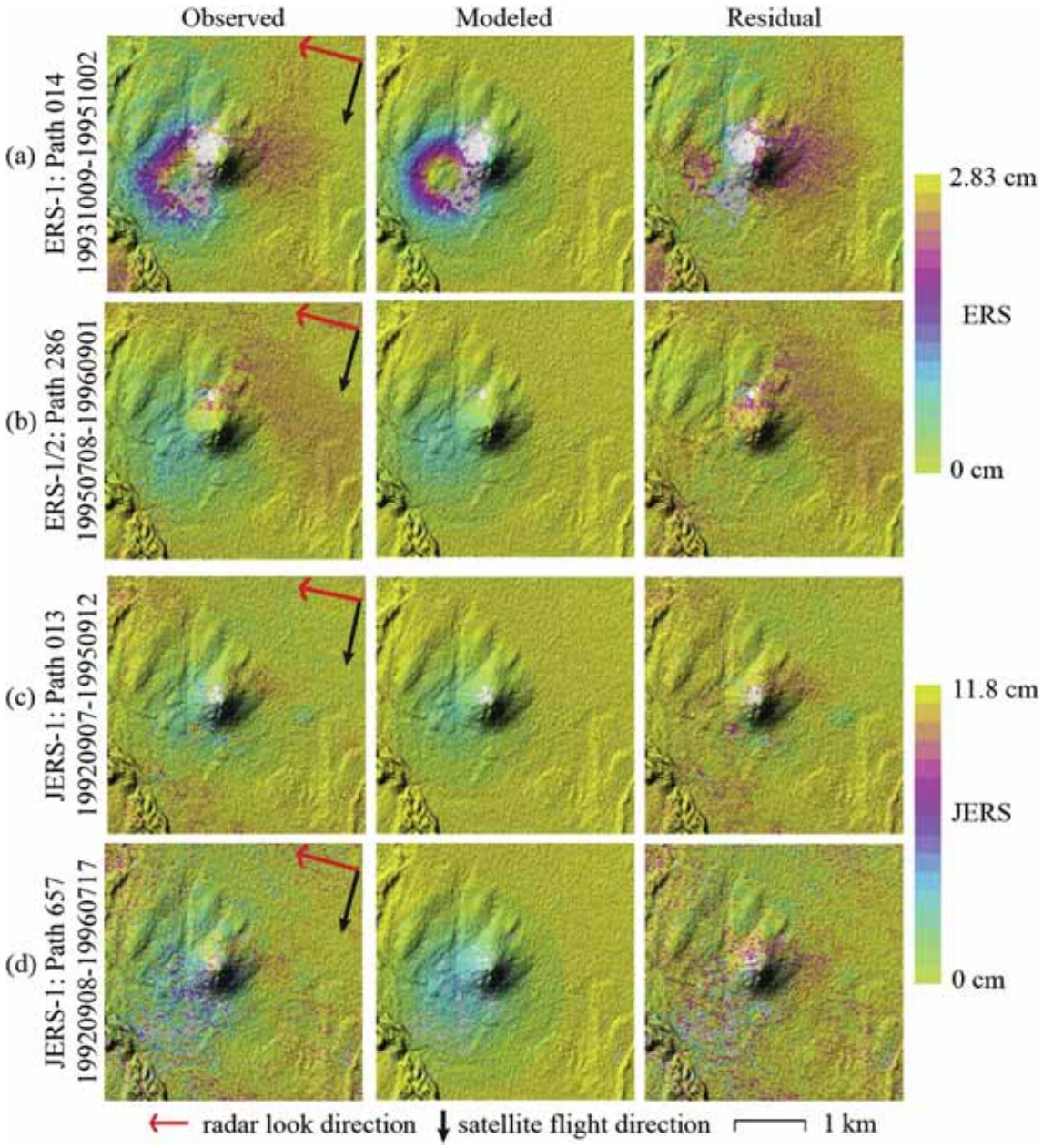

Fig. 6. Examples of observed interferograms (left), synthetic interferograms based on a best-fit prolate ellipsoid model, and residual interferograms (right) during the pre-eruptive period (1992–1996) at Shrub mud volcano. (a) ERS-1 path 014, ~2 yr interval; (b) ERS1/2 path 286, ~1 yr interval; (c) JERS-1 path 013, ~3 yr interval; (d) JERS-1 path 657, ~4 yr interval. See Table 1 for additional information.

median depths below Shrub's summit of 0.74 km and 0.65 km (Table 2), respectively. Fig. 5c shows a WSW-ENE topographic profile across both sources, which are shown schematically (depths and dimensions not accurate) to illustrate their locations relative to the summit and a low topographic mound on the southwest flank (more on that later). Representative examples of observed, modeled, and residual interferograms

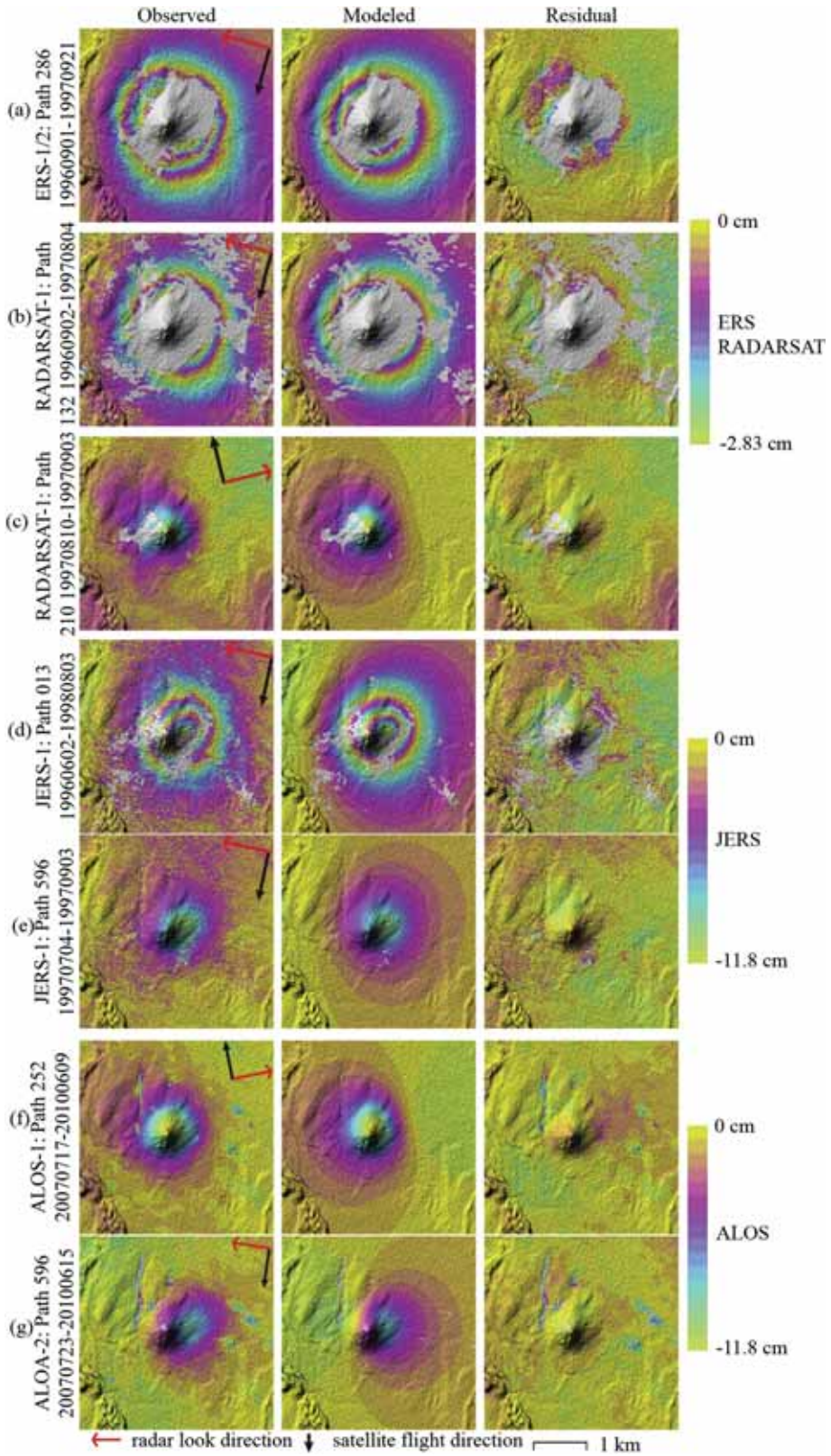

Fig. 7. Examples of observed interferograms (left), synthetic interferograms based on a best-fit prolate spheroid model (middle), and residual interferograms (right) for 7 satellite paths (see Table 1). (a) ERS1/2 path 286, ~1 yr interval; (b) RADARSAT-1 path 132, ~1 yr interval; (c) RADARSAT-1 path 210, ~1-month interval; (d) JERS-1 path 013, ~2 yr interval; (e) JERS-1 path 657, ~2 months interval; (f) ALOS PALSAR path 252, ~3 yr interval; (g) ALOS PALSAR path 596, ~3 yr interval.

for pre-eruptive (1992–1996) and coeruptive (1996–2000 and 2006–2011) time periods, using the refined source locations described above, are shown in Figs. 6 and 7, respectively.

It should be noted that the Yang model encountered some limitations due to the shallower source in this study. The Yang et al. (1988) spheroidal source only works in a relatively simple geometry, and it is only valid when the source depth is greater than twice the radius of curvature of the source. For example, if the source is oriented with its semi-major axis (a) parallel the vertical-axis (i.e., the semi-major axis is perpendicular to the free surface), the source depth must be greater or equal to $2 * a$. In our case, the depth of 0.65 km is not larger than $2 * 0.44 = 0.88$ km. When the source depth is too shallow, the Yang model does not accurately predict the near-field surface displacement. Moreover, the material properties may change rapidly along depth, when the source depth is shallow, while the model assumes a homogeneous medium. Therefore, all these can impact the model results: the source depth and the volume change may have deviations from the truth even though the fitting is good (Figs. 7 and 8). Solutions to the above limitations should come from finite element model or boundary element method (e.g., Davis et al. (2017)). As an InSAR image captures both the near-field and the far-field deformation patterns, our results and the depiction of the magma plumbing system at Shrub should be generally correct despite the limitations of the model.

3.3. Source-volume change time series

To estimate source volume changes over time, we use a least squares approach similar to that used by other authors to retrieve a deformation history from sets of interferograms that overlap in time (e.g., Lu et al. (2005); Berardino et al. (2002)). In addition to providing a smoothed history from temporally overlapping interferograms, the approach reduces the effects of atmospheric artifacts. Such artifacts usually are associated with particular epochs and are not spatially correlated through time. There is no overlapping coverage during the ~6-year gap in observations from 2000 to 2006, so we analyze two groups of interferograms separately and extrapolated across the gap. The 1992–2000 group includes interferograms from ERS-1 path 014, ERS-1/2 path 286, JERS-1 paths 013 and 657, and RADATSAT-1 paths 132 and 210 (Fig. 8a). The 2006–2011 group includes ALOS PALSAR paths 252 and 596 (Fig. 8b).

We estimate the cumulative source volume changes as a function of time for each satellite path by accumulating incremental changes derived from individual but temporally overlapping interferograms, using the least squares approach described above. Results are consistent among the various satellites and paths. The southwest flank source inflated steadily during the pre-eruptive phase from the first observation in July 1992 until May 1996. The summit source deflated at a varying rate from June 1996, when eruptive activity was first reported, until May 2000 when the 6-year gap in coverage begins (Fig. 8a, c). The deflationary trend continued at a lower average rate during the May 2006–March 2011 observation window (Fig. 8b, c).

The results suggest activity can be subdivided into one pre-eruptive inflation phase (July 1992–May 1996) and five coeruptive deflation phases based on differing average rates of volume loss (July 1996–May 1997, June 1997–December 1997, January 1998–August 1998, September 1998–May 2000, and May 2006–March 2011). We calculate average volume-change rates for each of those intervals by fitting a least squares line to the data (Fig. 8).

The average rate of volume increase beneath Shrub's southwest flank during the pre-eruptive period covered by our study (~4 years) was 0.35×10^5 m^3/yr. During the coeruptive period, the rate of summit

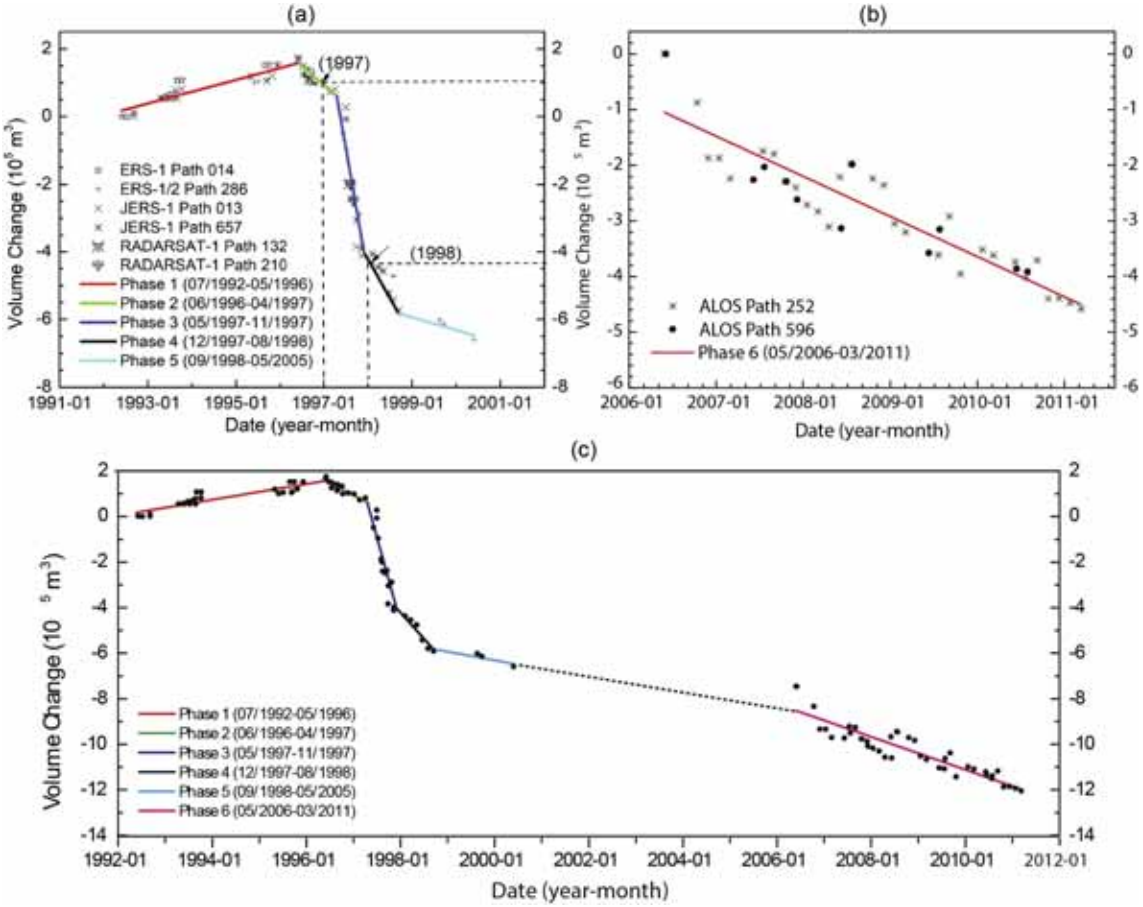

Fig. 8. Time series of estimated volume changes in the combined flank + summit sources described in the text, with linear fits showing average rates. (a) July 1992–May 2000; (b) May 2006–March 2011; (c) July 1992–March 2011. Satellites and orbital paths for individual interferograms are shown in lower left of each panel.

source-volume decrease was greatest during May–November 1997 (~8.71 × 10^5 m^3/yr), consistent with field observations of strong eruptive activity during that period (McGimsey and Wallace, 1999). The calculated volume loss from the summit source from the beginning of 1997 to its end was about 540,000 m^3 (Fig. 8a). Based on field visits in June 1997 and August 1997 (Richter et al., 1998) reported: "More than 500,000 m^3 of mud have been erupted since activity began in the spring of 1997" (see also McGimsey et al. (2004); https://www.avo.alaska.edu/volcanoes/activity.php?volcname=Klawasi%20Group&eruptionid=340&page=basic].

4. Discussion and conceptual model

Mud volcanism in sedimentary settings is well-studied owing to its implications for petroleum exploration, seismicity, geohazards, and the impact on climate of greenhouse gases including CO_2 and CH_4 (Mazzini and Etiope, 2017). Less attention has been paid to the workings of mud volcanoes fueled by magmatic, plutonic, or hydrothermal heat. However, some of the same physical principles must apply to both classes of features. Mazzini and Etiope (2017, p. 101) contend that four processes are essential for sedimentary volcanism: gravitational instability (buoyancy), fluid overpressure, hydrofracturing, and fluid flow along permeable pathways. The same is likely true for mud volcanism in volcanic settings, where heat and acid gases promote alteration of host rock to clays that can mix with groundwater to form buoyant mud, self-sealing of microfractures by ductile flow or mineral deposition can lead to fluid overpressures (Fournier, 2007), and fracture permeability can be created by hydrofracturing or seismic swarms that are common in settings like Yellowstone.

Surface deformation has been documented at LUSI mud volcano in Indonesia (Abidin et al., 2009; Aoki and Sidiq, 2014; Fukushima et al., 2009; Rudolph et al., 2013) and at the Ayaz–Akhtarma mud volcanoes in the Azerbaijan mud volcano group (Antonielli et al., 2014; Hommels et al., 2003; Mellors et al., 2005). Abidin et al. (2009) reported simultaneous uplift and subsidence during the LUSI eruption. They proposed subsidence was caused by collapse of the overburden due to removal of mud from the subsurface, and attributed uplift to localized vertical movement on the Watukosek fault system. Faulting also seems to play a role in deformation at the Ayaz–Akhtarma mud volcanoes, where faults/fractures separate sectors with different rates of uplift or subsidence.

At Shrub mud volcano, we observed subtle inflation prior to the onset of vigorous eruptive activity and subsidence during that activity, suggesting a deformation pattern similar to those observed at many magmatic volcanoes (Dzurisin, 2007). However, at first glance it seems odd that: (1) the center of pre-eruptive inflation was offset from the eventual vent area, (2) no pre-eruptive inflation was observed in the summit area, which deflated during the eruption, and (3) the flank source did not also deflate during the eruption. All three observations can be explained by the following conceptual model, which although not verifiable with existing data seems nonetheless plausible (Fig. 9).

The absence of pre-eruptive summit inflation can be explained if the conduit was pressurized to near its rupture threshold prior to the first SAR observation in 1992. We surmise the conduit ruptured laterally before that date and was feeding an expanding sill under the southwest flank when SAR observations began (Fig. 9a). Because the mud supply was accommodated by the growing sill, the conduit did not inflate further during the first ~4 years of SAR observations. Rather, it began deflating rapidly in summer 1996 when it ruptured upward and began conveying the entire mud supply to the surface (Fig. 9b). The sill stopped expanding as a consequence, but it did not deflate because the weight of the thin overburden was not great enough to squeeze mud back out; it became a permanent addition to the edifice. We did

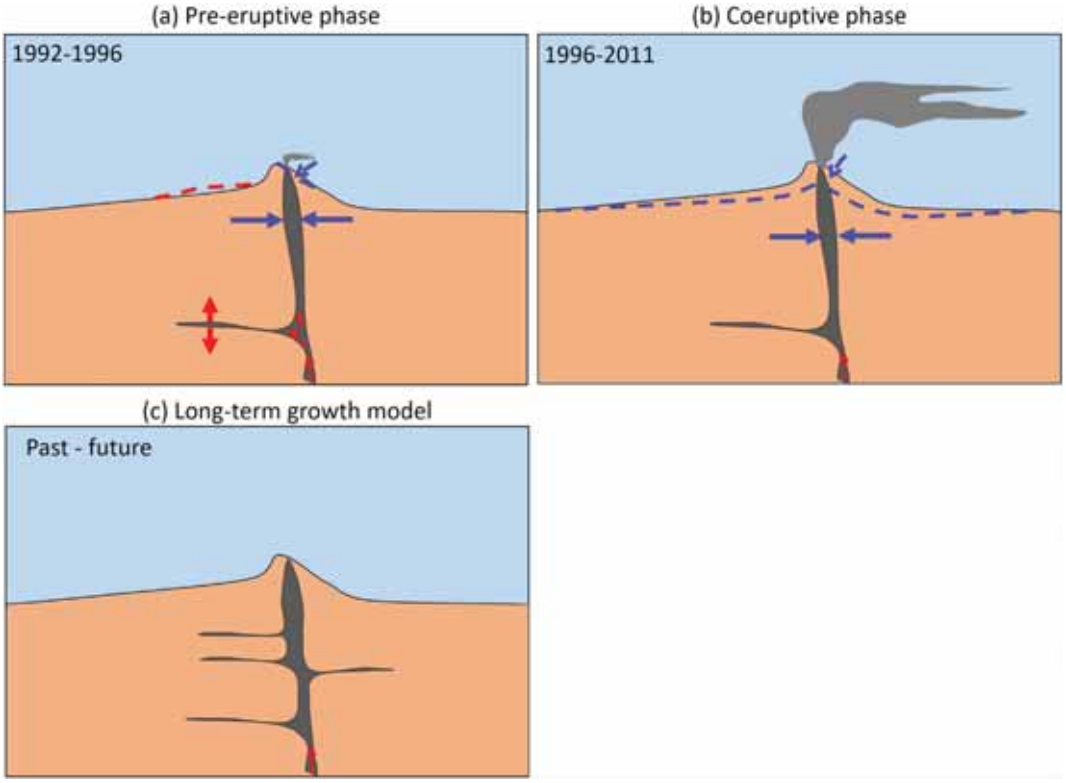

Fig. 9. Conceptual model of activity at Shrub mud volcano. (a) During the pre-eruptive phase starting with the first SAR observation in 1992, mud supplied to the volcano from below fed an expanding sill beneath the southwest flank, causing surface inflation there. A near-vertical conduit beneath the summit had pressurized and filled with mud beforehand. (b) In summer 1996, the conduit ruptured to the surface and began deflating at a rate that diminished over time. The sill under the southwest flank stopped growing but did not deflate because the weight of the thin overburden was insufficient to cause mud to withdraw.

not attempt to model the slight amount of pre-eruptive subsidence observed on the east flank, but we suggest it might indicate slow cooling or dewatering of deposits from earlier activity.

Our conceptual model has implications for both past and future activity at Shrub. As shown schematically in Fig. 5c, our model sill lies directly under a low topographic mound on the volcano's southwest flank. This suggests to us that lateral injections of mud with attendant uplift there might be a common feature of past activity, to the extent they are recorded in the modern topography (Fig. 9c). In that regard, recall it was the southwest flank where (Nichols and Yehle, 1961) observed minor eruptive activity during their visit in 1955; perhaps that flank and the summit area have been the most active parts of the volcano in recent time.

If our inference that an expanding sill was accommodating the mud supply to Shrub prior to the onset of eruptive activity, that the inflation rate of the sill (0.35×10^5 m^3/yr) might approximate the long-term supply rate. The summit deflation rate during the 2006–2011 observation window had slowed to about twice that value (0.95×10^5 m^3/yr), suggesting activity might have been approaching a steady state. Unfortunately, we are not aware of any more recent observations of Shrub to test that idea.

5. Conclusion

In the absence of ground-based monitoring systems and detailed historical information, InSAR observations of mud volcanoes in Alaska and elsewhere can play a useful role in documenting eruptive activity and forecasting associated hazards. Such is the case at Shrub, where our study provides a framework for interpreting recent eruptive activity and suggests it could continue at the current level for the foreseeable future, with attendant hazards posed by hot unstable ground and CO2 emissions.

In this study, we have used the archive of InSAR data to characterize the ground deformation at Shrub before, during, and after its reactivation, spanning 1992–2000 and 2006–2011. The InSAR results show that Shrub's southwest flank slowly inflated from the first SAR observation in 1992 until mid-1996, its summit area dramatically deflated spanning mid-1996 to 1999, and then continued deflating at relatively slow rates from 2006 to 2011.

We fit these observations with two deformation sources: a deflating, steeply dipping, closed pipe-like body under the summit area, and an inflating, shallow-dipping, sill-like body under the southwest flank. Both sources are shallow, with centroids less than 1 km beneath the summit. The source-volume changes over time clearly show that the volume-inflated rate is much less than the volume-deflated rates during eruption.

We interpret the summit source as the volcano's feeder conduit, which pressurized prior to the first SAR observation in 1992. We also infer that before 1992, the conduit ruptured to feed a lateral intrusion of mud under the southwest flank, perhaps along a bedding plane in underlying glaciolacustrine deposits. The growing sill caused the southwest flank to inflate while it accommodated the mud supply from depth, explain our observations of pre-eruptive inflation on the southwest flank but not the summit. The summit began deflating when the conduit ruptured to the surface at the onset of eruptive activity. The flank source did not deflate concurrently because the weight of the thin overburden was insufficient to collapse the sill. There is a suggestion in the modern topography that lateral intrusions under Shrub's southwest flank are a common feature of activity there.

Acknowledgments

Roger Denlinger provided helpful insights into the conceptual model for activity at Shrub presented here. Constructive comments from two anonymous reviewers and the Editor-in-Chief improved the manuscript. ERS-1 and ERS-2, JERS-1 and ALOS APLSAR, and RADARSAT-1 SAR images are copyright 1991–2011 European Space Agency (ESA), Japan Aerospace Exploration Agency (JAXA), and Canadian Space Agency (CSA), respectively, and were provided by the Alaska Satellite Facility (ASF) and JAXA. AW3D DEM is also provided by JAXA. We thank ASF for the excellent support in providing the JERS-1 imagery. This research was supported by China Scholarship Council, National Natural Science Foundation of China (Grant No. 41731066, 41790445, 41874005), Natural Science Basic Research Plan in Shaanxi Province of China (2018JQ4031), the Fundamental Research Funds for the Central Universities, CHD (No. 300102269303, 300102269207), and Shuler-Foscue endowment at the Southern Methodist University.

References

Abidin, H., Davies, R.J., Kusuma, M., Andreas, H., Deguchi, T., 2009. Subsidence and uplift of Sidoarjo (East Java) due to the eruption of the Lusi mud volcano (2006–present). Environ. Geol. 57, 833–844. https://doi.org/10.1007/s00254-008-1456-0.

Amelung, F., Jónsson, S., Zebker, H., Segall, P., 2000. Widespread uplift and 'trapdoor' faulting on Galapagos volcanoes observed with radar interferometry. Nature 407, 993. https://doi.org/10.1038/35039604.

Antonielli, B., Monserrat, O., Bonini, M., Righini, G., Sani, F., Luzi, G., Feyzullayev, A.A., Aliyev, C.S., 2014. Pre-eruptive ground deformation of Azerbaijan mud volcanoes detected through satellite radar interferometry (DInSAR). Tectonophysics 637, 163–177. https://doi.org/10.1016/j.tecto.2014.10.005.

Aoki, Y., Sidiq, T.P., 2014. Ground deformation associated with the eruption of Lumpur Sidoarjo mud volcano, East Java, Indonesia. J. Volcanol. Geotherm. Res. 278, 96–102. https://doi.org/10.1016/j.jvolgeores.2014.04.012.

Battaglia, M., Segall, P., Murray, J., Cervell, P., Langbein, J., 2003. The mechanics of unrest at Long Valley caldera, California: 1. Modeling the geometry of the source using GPS, leveling and two-color EDM data. J. Volcanol. Geotherm. Res. 127, 195–217. https://doi.org/10.1016/S0377-0273(03)00171-9.

Battaglia, M., Cervelli, P.F., Murray, J.R., 2013. dMODELS: a MATLAB software package for modeling crustal deformation near active faults and volcanic centers. J. Volcanol. Geotherm. Res. 254, 1–4. https://doi.org/10.1016/j.jvolgeores.2012.12.018.

Berardino, P., Fornaro, G., Lanari, R., Sansosti, E., 2002. A new algorithm for surface deformation monitoring based on small baseline differential SAR interferograms. IEEE Trans. Geosci. Remote Sens. 40, 2375–2383. https://doi.org/10.1109/TGRS.2002.803792.

Biggs, J., Lu, Z., Fournier, T., Freymueller, J.T., 2010. Magma flux at Okmok Volcano, Alaska, from a joint inversion of continuous GPS, campaign GPS, and interferometric synthetic aperture radar. Journal of Geophysical Research: Solid Earth 115. https://doi.org/10.1029/2010JB007577.

Binder, K., Heermann, D., Roelofs, L., Mallinckrodt, A.J., McKay, S., 1993. Monte Carlo simulation in statistical physics. Comput. Phys. 7, 156–157. https://aip.scitation.org/doi/pdf/10.1063/1.4823159.

Bishop, R.S., 1978. Mechanism for emplacement of piercement diapirs. AAPG Bull. 62, 1561–1583. http://archives.datapages.com/data/bulletns/1977-79/data/pg/0062/0009/1550/1561.htm.

Bonaccorso, A., Davis, P.M., 1999. Models of ground deformation from vertical volcanic conduits with application to eruptions of Mount St. Helens and Mount Etna. J Geophys Res-Sol Ea 104, 10531–10542. https://doi.org/10.1029/1999JB900054.

Brown, K.M., 1990. The nature and hydrogeologic significance of mud diapirs and diatremes for accretionary systems. Journal of Geophysical Research: Solid Earth 95, 8969–8982. https://doi.org/10.1029/JB095iB06p08969.

Chiodini, G., D'Alessandro, W., Parello, F., 1996. Geochemistry of gases and waters discharged by the mud volcanoes at Paternò, Mt. Etna (Italy). Bull. Volcanol. 58, 51–58. https://doi.org/10.1007/s004450050.

Davis, T., Healy, D., Bubeck, A., Walker, R., 2017. Stress concentrations around voids in three dimensions: the roots of failure. J. Struct. Geol. 102, 193–207. https://doi.org/10.1016/j.jsg.2017.07.013.

Dvorak, J.J., Dzurisin, D., 1997. Volcano geodesy: the search for magma reservoirs and the formation of eruptive vents. Rev. Geophys. 35, 343–384. https://doi.org/10.1029/97RG00070.

Dzurisin, D., 2007. Volcano Deformation – Geodetic Monitoring Techniques. Springers, Springer-Praxis Books in Geophysical Sciences, Berlin https://www.springer.com/us/book/9783540426424.

Ebmeier, S., Biggs, J., Mather, T., Elliott, J., Wadge, G., Amelung, F., 2012. Measuring large topographic change with InSAR: lava thicknesses, extrusion rate and subsidence rate at Santiaguito volcano, Guatemala. Earth Planet. Sci. Lett. 335, 216–225. https://doi.org/10.1016/j.epsl.2012.04.027.

Fialko, Y., Simons, M., 2001. Evidence for on-going inflation of the Socorro magma body, New Mexico, from interferometric synthetic aperture radar imaging. Geophys. Res. Lett. 28, 3549–3552. https://doi.org/10.1029/2001GL013318.

Fialko, Y., Khazan, Y., Simons, M., 2001. Deformation due to a pressurized horizontal circular crack in an elastic half-space, with applications to volcano geodesy. Geophys. J. Int. 146, 181–190. https://doi.org/10.1046/j.1365-246X.2001.00452.x.

Fournier, R.O., 2007. Hydrothermal Systems and Volcano Geochemistry, Volcano Deformation. Springer, pp. 323–341. https://link.springer.com/chapter/10.1007/978-3-540-49302-0_10.

Fukushima, Y., Mori, J., Hashimoto, M., Kano, Y., 2009. Subsidence associated with the LUSI mud eruption, East Java, investigated by SAR interferometry. Mar. Pet. Geol. 26, 1740–1750. https://doi.org/10.1016/j.marpetgeo.2009.02.001.

Hedberg, H.D., 1974. Relation of methane generation to undercompacted shales, shale diapirs, and mud volcanoes. AAPG Bull. 58, 661–673. http://archives.datapages.com/data/bulletns/1974-76/data/pg/0058/0004/0650/0661.htm.
Hommels, A., Scholte, K., Munoz-Sabater, J., Hanssen, R., Van der Meer, F., Kroonenberg, S., Aliyeva, E., Huseynov, D., Guliev, I., 2003. Preliminary Aster and InSAR imagery combination for mud volcano dynamics, Azerbaijan. International Geoscience and Remote Sensing Symposium, pp. 1573–1575 pp. III.
Hooper, A., 2008. A multi-temporal InSAR method incorporating both persistent scatterer and small baseline approaches. Geophys. Res. Lett. 35. https://doi.org/10.1029/2008GL034654.
Kioka, A., Ashi, J., 2015. Episodic massive mud eruptions from submarine mud volcanoes examined through topographical signatures. Geophys. Res. Lett. 42, 8406–8414. https://doi.org/10.1002/2015GL065713.
Kopf, A.J., 2002. Significance of mud volcanism. Rev. Geophys. 40. https://doi.org/10.1029/2000RG000093.
Langbein, J.O., 2003. Deformation of the Long Valley Caldera, California: inferences from measurements from 1988 to 2001. J. Volcanol. Geotherm. Res. 127, 247–267. https://doi.org/10.1016/S0377-0273(03)00172-0.
Lu, Z., Dzurisin, D., 2014. InSAR Imaging of Aleutian Volcanoes, InSAR Imaging of Aleutian Volcanoes. Springer, pp. 87–345. https://link.springer.com/chapter/10.1007/978-3-642-00348-6_6.
Lu, Z., Masterlark, T., Dzurisin, D., Rykhus, R., Wicks, C., 2003. Magma supply dynamics at Westdahl volcano, Alaska, modeled from satellite radar interferometry. Journal of Geophysical Research: Solid Earth 108. https://doi.org/10.1029/2002JB002311.
Lu, Z., Masterlark, T., Dzurisin, D., 2005. Interferometric synthetic aperture radar study of Okmok volcano, Alaska, 1992–2003: magma supply dynamics and postemplacement lava flow deformation. Journal of Geophysical Research: Solid Earth 110. https://doi.org/10.1029/2004JB003148.
Lu, Z., Dzurisin, D., Wicks, C., Power, J., Kwoun, O., Rykhus, R., 2007. Diverse deformation patterns of Aleutian volcanoes from satellite interferometric synthetic aperture radar (InSAR). Volcanism and subduction: the Kamchatka region, 249–261 https://doi.org/10.1029/172GM18.
Lu, Z., Dzurisin, D., Biggs, J., Wicks, C., McNutt, S., 2010. Ground surface deformation patterns, magma supply, and magma storage at Okmok volcano, Alaska, from InSAR analysis: 1. Intereruption deformation, 1997–2008. Journal of Geophysical Research: Solid Earth 115. https://doi.org/10.1029/2009JB006969.
Massonnet, D., Feigl, K.L., 1998. Radar interferometry and its application to changes in the Earth's surface. Rev. Geophys. 36, 441–500. https://doi.org/10.1029/97RG03139.
Mazzini, A., Etiope, G., 2017. Mud volcanism: an updated review. Earth-Sci. Rev. 168, 81–112. https://doi.org/10.1016/j.earscirev.2017.03.001.
Mazzini, A., Svensen, H., Akhmanov, G., Aloisi, G., Planke, S., Malthe-Sørenssen, A., Istadi, B., 2007. Triggering and dynamic evolution of the LUSI mud volcano, Indonesia. Earth Planet. Sci. Lett. 261, 375–388. https://doi.org/10.1016/j.epsl.2007.07.001.
Mazzini, A., Nermoen, A., Krotkiewski, M., Podladchikov, Y., Planke, S., Svensen, H., 2009. Strike-slip faulting as a trigger mechanism for overpressure release through piercement structures. Implications for the Lusi mud volcano, Indonesia. Mar. Pet. Geol. 26, 1751–1765. https://doi.org/10.1016/j.marpetgeo.2009.03.001.
McGimsey, R.G., Wallace, K.L., 1999. 1997 Volcanic Activity in Alaska and Kamchatka: Summary of Events and Response of the Alaska Volcano Observatory. U.S. Geological Survey, https://pubs.usgs.gov/of/1999/0448/pdf/1997SummaryofEventsAVO.pdf.
McGimsey, R.G., Neal, C.A., Girina, O., 2004. 1999 volcanic activity in Alaska and Kamchatka: summary of events and response of the Alaska Volcano Observatory. U.S. Geological Survey, https://pubs.usgs.gov/of/2004/1033/1999VolcanicActivityAlaska.pdf.
Mellors, R.J., Bunyapanasarn, T., Panahi, B., 2005. InSAR Analysis of the Absheron Peninsula and Nearby Areas, Azerbaijan, Mud Volcanoes, Geodynamics and Seismicity. Springer, pp. 201–209. https://link.springer.com/chapter/10.1007%2F1-4020-3204-8_18?LI=true.
Mellors, R., Kilb, D., Aliyev, A., Gasanov, A., Yetirmishli, G., 2007. Correlations between earthquakes and large mud volcano eruptions. Journal of Geophysical Research: Solid Earth 112. https://doi.org/10.1029/2006JB004489.
Motyka, R.J., Poreda, R.J., Jeffrey, A.W., 1989. Geochemistry, isotopic composition, and origin of fluids emanating from mud volcanoes in the Copper River basin, Alaska. Geochim. Cosmochim. Acta 53, 29–41. https://doi.org/10.1016/0016-7037(89)90270-6.
Nichols, D.R., Yehle, L.A., 1961. Mud Volcanoes in the Copper River Basin. University of Toronto Press, Alaska.
Pagli, C., Wright, T.J., Ebinger, C.J., Yun, S.-H., Cann, J.R., Barnie, T., Ayele, A., 2012. Shallow axial magma chamber at the slow-spreading Erta Ale Ridge. Nat. Geosci. 5, 284. https://doi.org/10.1038/ngeo1414.
Patrick, M., Dean, K., Dehn, J., 2004. Active mud volcanism observed with Landsat 7 ETM +. J. Volcanol. Geotherm. Res. 131, 307–320. https://doi.org/10.1016/S0377-0273(03)00383-4.
Pitt, A.M., Hutchinson, R.A., 1982. Hydrothermal changes related to earthquake activity at mud volcano, Yellowstone-National-Park, Wyoming. J. Geophys. Res. 87, 2762–2766. https://doi.org/10.1029/JB087iB04p02762.
Pritchard, M.E., Simons, M., 2004. An InSAR-based survey of volcanic deformation in the southern Andes. Geophys. Res. Lett., 31 https://doi.org/10.1029/2004GL020545.
Richter, D.H., Symonds, R., Rosenkrans, D., McGimsey, R., Evans, W.C., Poreda, R., 1998. Report on the 1997 Activity of Shrub Mud Volcano, Wrangell-St. Elias National Park and Preserve, Southcentral Alaska. U.S. Geological Survey, https://doi.org/10.3133/ofr98128.
Rosen, P.A., Hensley, S., Joughin, I.R., Li, F.K., Madsen, S.N., Rodriguez, E., Goldstein, R.M., 2000. Synthetic aperture radar interferometry. Proc. IEEE 88, 333–382. https://doi.org/10.1109/5.838084.
Rudolph, M., Shirzaei, M., Manga, M., Fukushima, Y., 2013. Evolution and future of the Lusi mud eruption inferred from ground deformation. Geophys. Res. Lett. 40, 1089–1092. https://doi.org/10.1002/grl.50189.
Santillan, J., Makinano-Santillan, M., 2016. Vertical accuracy assessment of 30-m resolution ALOS, ASTER, and SRTM global dems over Northeastern Mindanao, Philippines. International Archives of the Photogrammetry. Remote Sensing & Spatial Information Sciences 41. https://doi.org/10.5194/isprs-archives-XLI-B4-149-2016.
Sheppard, D., Truesdell, A., Janik, C., 1992. Geothermal gas compositions in yellowstone National Park, USA. J. Volcanol. Geotherm. Res. 51, 79–93. https://doi.org/10.1016/0377-0273(92)90061-H.
Sorey, M.L., Werner, C., McGimsey, R.G., Evans, W., 2000. Hydrothermal activity and carbon-dioxide discharge at Shrub and Upper Klawasi mud volcanoes, Wrangell Mountains, Alaska. U.S. Geological Survey, https://pubs.usgs.gov/wri/wri004207/pdf/wri004207.pdf.
Tiampo, K.F., Rundle, J.B., Fernandez, J., Langbein, J.O., 2000. Spherical and ellipsoidal volcanic sources at Long Valley caldera, California, using a genetic algorithm inversion technique. J. Volcanol. Geotherm. Res. 102, 189–206. https://doi.org/10.1016/S0377-0273(00)00185-2.
Vanderkluysen, L., Burton, M.R., Clarke, A.B., Hartnett, H.E., Smekens, J.F., 2014. Composition and flux of explosive gas release at LUSI mud volcano (East Java, Indonesia). Geochem. Geophys. Geosyst. 15, 2932–2946. https://doi.org/10.1002/2014GC005275.
Wang, C.Y., Manga, M., 2010. Hydrologic responses to earthquakes and a general metric. Geofluids 10, 206–216. https://doi.org/10.1111/j.1468-8123.2009.00270.x.
White, D.E., 1955. Violent mud-volcano eruption of Lake City hot springs, northeastern California. Geol. Soc. Am. Bull. 66, 1109–1130. https://doi.org/10.1130/0016-7606(1955)66[1109:VMEOLC]2.0.CO;2.
Wicks, C.W., Dzurisin, D., Ingebritsen, S., Thatcher, W., Lu, Z., Iverson, J., 2002. Magmatic activity beneath the quiescent Three Sisters volcanic center, central Oregon Cascade Range, USA. Geophys. Res. Lett. 29. https://doi.org/10.1029/2001GL014205.
Williams, C.A., Wadge, G., 1998. The effects of topography on magma chamber deformation models: application to Mt. Etna and radar interferometry. Geophys. Res. Lett. 25, 1549–1552. https://doi.org/10.1029/98GL01136.
Wright, T.J., Ebinger, C., Biggs, J., Ayele, A., Yirgu, G., Keir, D., Stork, A., 2006. Magma-maintained rift segmentation at continental rupture in the 2005 Afar dyking episode. Nature 442, 291. https://doi.org/10.1038/nature04978.
Yang, X.M., Davis, P.M., Dieterich, J.H., 1988. Deformation from inflation of a dipping finite prolate spheroid in an elastic half-space as a model for volcanic stressing. J Geophys Res-Solid 93, 4249–4257. https://doi.org/10.1029/JB093iB05p04249.
Yang, X.M., Davis, P.M., Delaney, P.T., Okamura, A.T., 1992. Geodetic analysis of dike intrusion and motion of the magma reservoir beneath the summit of Kilauea Volcano, Hawaii – 1970–1985. J Geophys Res-Sol Ea 97, 3305–3324. https://doi.org/10.1029/91JB02842.